ADVANCED FUNCTIONAL MATERIALS
www.afm-journal.de

Influence of MXene Interlayer Spacing on the Interaction with Microwave Radiation

Roman Rakhmanov, Stefano Ippolito, Marley Downes, Alex Inman, Jamal AlHourani, James Fitzpatrick, Yury Gogotsi, and Gary Friedman**

The origin of MXene's excellent electromagnetic shielding performance is not fully understood. MXene films, despite being inhomogeneous at the nanometer scale, are often treated as if they are compared to bulk conductors. It is reasonable to wonder if the treatment of MXene as a homogeneous material remains valid at very small film thickness and if it depends on the interlayer spacing. The goal of the present work is to test if the homogeneous material model is applicable to nanometer-thin $Ti_3C_2T_x$ MXene films and, if so, to investigate how the model parameters may depend on variations in MXene interlayer spacings. MXene films containing flakes with interlayer spacing between 1.9 and 5.5 Å have been prepared using various intercalating agents. It is shown that modeling the films as being homogeneous agrees with experimental tests in the microwave frequency range. Microwave conductivity and dielectric constant parameters are estimated for the homogeneous film model by fitting measured results. The direct current (DC) conductivity matches the estimated microwave conductivity on the order of magnitude. A highly effective dielectric constant provides a good fit for the lower conductivity MXene films. Optical absorption agrees with the homogeneous material model of thin films as well.

1. Introduction

MXenes are a class of 2D transition metal carbides, nitrides, and/or carbonitrides with the general formula of $M_{n+1}X_nT_x$, where M is an early transition metal[1–4] (e.g., Ti, V, Nb, etc.), X is C and/or N, and n ranges from 1 to 4. MXenes have received ever-growing attention due to their versatile properties, such as high metallic conductivity (exceeding 2.4×10^6 S m^{-1}),[5,6] low infrared emissivity,[7] tunable chemistry, as well as hydrophilicity, promoting cost-effective MXene processing from aqueous dispersions and deposition on a wide variety of surfaces.[8] In particular, $Ti_3C_2T_x$, the most studied and stable MXene, shows relatively high conductivity and environmental stability.[9] These properties brought MXenes into the spotlight for technologies such as electromagnetic interference (EMI) shields and microwave circuit components.[10–12] Their EMI shielding properties are comparable to metals and exceed carbon and other nanomaterials reported in the literature thus far.[13–16] For instance, $Ti_3C_2T_x$ coatings applied onto 3D-printed polymeric waveguides display analogous performance to their metal counterparts but with a significant weight reduction.[17] It is also possible to incorporate MXenes into composites to produce multifunctional materials with high EMI shielding performance.[18–22] EMI shielding properties of MXenes are also tunable via electrochemical modulation.[18] Moreover, MXenes-based devices continue to perform well up to the THz frequencies.[23] Previous work[24] demonstrated the ability of nanometer-thick $Ti_3C_2T_x$ films to absorb up to 50% of incoming microwaves through impedance matching. The film impedance was estimated through microwave measurements showing conductivity within the error of direct current (DC) measurements and is comparable to values in the THz range reported previously.[25]

The interaction of spray-coated MXene films with electromagnetic fields generally shows behavior similar to a composite material with conducting inclusions and sputtered[26] or thermally evaporated[27] thin metal films made of percolating metal islands. For example, nanometer-thin MXene films perform as well as metal films with similar thicknesses, even though the intrinsic conductivity of bulk metals is higher. Nanometer-thick sputtered metal films of multiple islands, and their resistivity differs from that of bulk metal due to this morphology.[28–32] MXene films have some similarities since their metallic flakes[33] are separated from each other by functional groups and intercalants,[34–36] still allowing for effective inter-flake electron transport. Theoretical calculations predict bandlike transport in MXenes,[37–39] and it has been shown that two different mechanisms of inter- and intra-flake electron transport may be active.[34,40–42] The above analogies

R. Rakhmanov, J. AlHourani, G. Friedman
Department of Electrical and Computer Engineering
Drexel University
3141 Chestnut St, Philadelphia, PA 19104, USA
E-mail: gf29@drexel.edu
R. Rakhmanov, S. Ippolito, M. Downes, A. Inman, J. AlHourani, J. Fitzpatrick, Y. Gogotsi
A. J. Drexel Nanomaterials Institute and Department of Materials Science and Engineering
Drexel University
3141 Chestnut St, Philadelphia, PA 19104, USA
E-mail: gogotsi@drexel.edu
The ORCID identification number(s) for the author(s) of this article can be found under https://doi.org/10.1002/adfm.202410591

DOI: 10.1002/adfm.202410591

between nanometer-thin metal films and MXene films suggest that the material's nano- and micro-structure is crucially important in determining its interaction with electromagnetic fields.

However, while increasing the thickness of metal films changes their nanoscale architecture, MXene flakes maintain their 2D structure as the film thickness increases. This raises the possibility of modeling MXene films as being homogeneous.[43] Many composite materials are modeled as homogeneous media in their interaction with electromagnetic fields.[44,45] The idea behind the development of such models is to derive equations for fields averaged over many material inhomogeneities. Remarkably, these equations can have the same form as Maxwell's equations except for the use of effective permittivity and permeability, which could be complex-valued to account for energy losses. Such models also permit substantially simplifying modeling interface phenomena via boundary conditions on normal and tangential electric and magnetic fields. The validity of the homogeneous medium models can be experimentally tested by varying the film thickness, measuring electromagnetic wave reflection and transmission, and comparing the results to the model predictions.[46] In the process, it is possible to estimate the values of the homogeneous model parameters such as permittivity and conductivity. This process can be repeated for MXene having different spacing between their conductive layers to understand how such spacing might affect the homogenization assumption and the resulting parameters in the homogeneous medium model. In addition, measured DC conductivity is compared to the microwave conductivity estimated for the homogeneous medium model. Optical measurements can be used to confirm that certain material features remain unchanged after the intercalation of different molecules between the layers.[47,48]

In the present work, we tested if the homogeneous material model is applicable to nanometer-thin $Ti_3C_2T_x$ MXene films and investigated how the model parameters depend on variations in MXene interlayer spacings by intercalating cations with various sizes between the negatively surface-charged MXene flakes.

2. Results and Discussion

2.1. Morphological and Structural Properties of Spray-Coated Films

MXene dispersions were produced following previously reported protocols,[4,6,49] providing flakes whose typical $Ti_3C_2T_x$ structure is presented in **Figure 1**a. As such, flakes contained adsorbed Li^+ after delamination. We used lithium chloride (LiCl), tetramethylammonium hydroxide (TMAOH), and tetrabutylammonium hydroxide (TBAOH) to intercalate positively charged Li^+, TMA^+, and TBA^+ species (cations) between the MXene sheets and increase the interlayer spacing in MXene films. The as-produced dispersion of MXene flakes was split into separated containers to perform ion exchange with TMAOH and TBAOH (Figure 1b). The resulting solutions were spray-coated onto glass substrates (Figure 1b) to make films with different interlayer spacings, depending on the intercalant (Figure 1c). After spray coating, a set of LiCl films was treated with HCl to minimize the amount of water and eliminate lithium ions (i.e., protonated sample).

To confirm the change in interlayer spacing due to the intercalation of different ions, X-ray diffraction (XRD) was carried

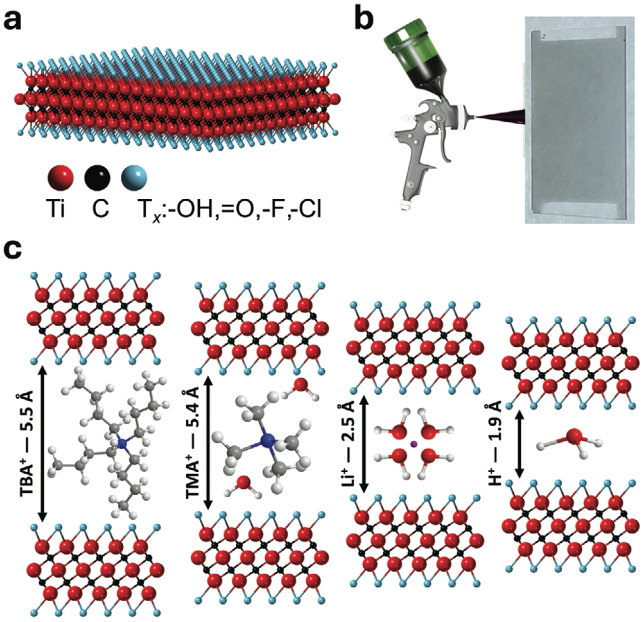

Figure 1. a) Sketch of $Ti_3C_2T_x$ structure, where red spheres represent Ti atoms, blackspheres are carbon atoms, and "T_x" are surface terminations represented in blue. b) Illustration of spray coating deposition of MXene aqueous dispersion and optical image of a typical spray-coated film on a glass slide of 24 × 40 × 0.15 mm. c) Illustration of $Ti_3C_2T_x$ layers intercalated with different cations, showing their interlayer spacing measured by XRD. Water molecules are shown in the interlayer spacing as red and white spheres.

out at ambient conditions on the spray-coated films. As seen in **Figure 2**a, all MXene films show the characteristic (002) peak, confirming the successful etching and delamination steps. The angular shift of the (002) peak is used to calculate the *d*-spacing, which accounts for the thickness of one MXene layer along with the surface groups and intercalants.[50] Interlayer spacing is calculated by subtracting the thickness of a single MXene layer, 9.4 Å, from the value of *d*-spacing. The LiCl-intercalated film shows the (002) peak located at 7.3°, resulting in a *d*-spacing of 12 Å, which implies an interlayer spacing of ≈2.6 Å, corresponding to a monolayer of water between the sheets.[50] To create the protonated sample, a LiCl-intercalated film (Figure S1, Supporting Information) was washed in HCl to remove lithium ions, producing the protonated sample. The interlayer spacing decreased to 1.9 Å as Li^+ and some water were removed from the sample. Vacuum annealing did not affect the *c*-lattice parameter of the protonated sample, indicating strong adhesion of water between the sheets (Figure S1, Supporting Information). The larger (002) peak shift of the TMAOH (at 5.9 °) and TBAOH (at 6.0 °) containing films confirm the intercalation of such large ions, resulting in larger *d*-spacings of 14.8 and 14.9 Å, respectively, providing interlayer spacings of 5.4 and 5.5 Å, similar to previously reported results.[35] Additionally, the intercalation of cetyltrimethylammonium bromide (CTAB) into the TMAOH film results in a further shift of the (002) peak toward lower 2θ, indicating expansion of the *d*-spacing (Figure S1, Supporting Information).

XRD confirmed successful control over the *d*-spacing and, thus, the potential to tune the interlayer spacing in $Ti_3C_2T_x$ films.

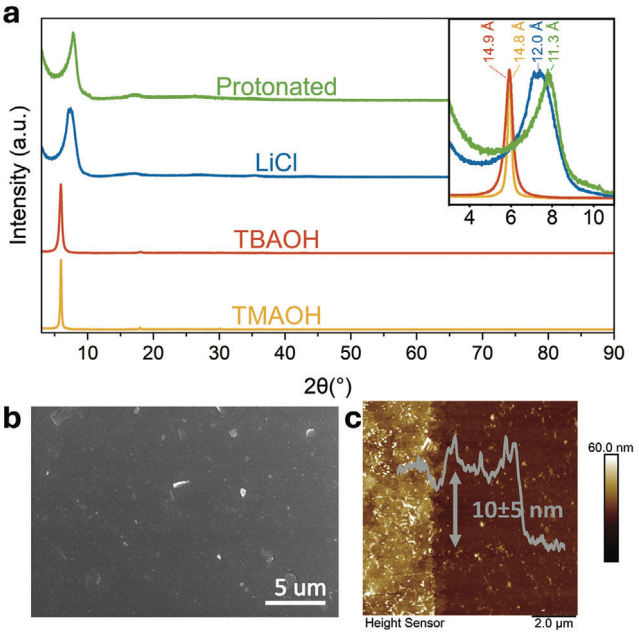

Figure 2. a) XRD patterns of $Ti_3C_2T_x$ films delaminated with LiCl and ion-exchanged using TMAOH, TBAOH, and HCl. The inset contains a zoomed-in region to highlight the (002) peak shift with a change in *d*-spacing values. b) Typical SEM and c) AFM images of the surface of a LiCl-intercalated film.

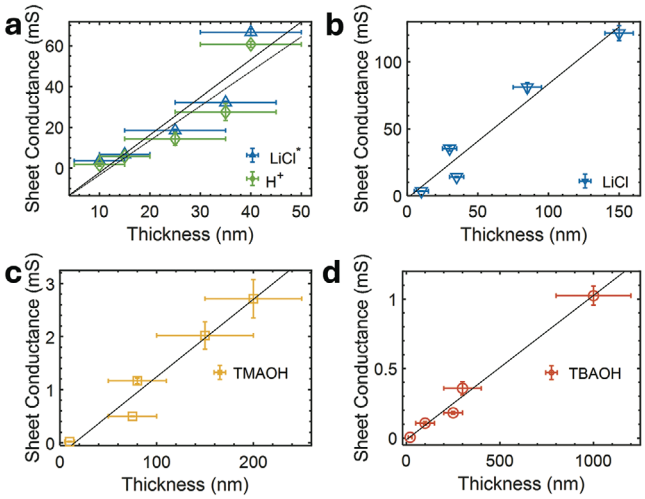

Figure 3. Sheet conductance of films as a function of film thickness for a) LiCl* and protonated films. Similar results are obtained despite a decrease in interlayer spacing of protonated samples. Linear slope provides a conductivity value of 18.4×10^5 and 17×10^5 S m^{-1} respectively, b) LiCl film with a conductivity value of 8.5×10^5 S m^{-1}, c) TMA-intercalated film conductivity of 1.4×10^4 S m^{-1}, d) TBA-intercalated film with a conductivity of 1.0×10^3 S m^{-1}. In all cases, linear dependence is observed, demonstrating bulk-like transport.

To explore the surface morphology of the films, they were analyzed using scanning electron microscopy (SEM) and atomic force microscopy (AFM). Figure 2b,c show continuous coverage of glass substrates with 10 nm-thick LiCl-intercalated film on micro- and nanoscales. With the increasing size of the intercalant agents, the continuous coverage of the substrate is maintained, but the surface roughness increases (Figure S1b,c, Supporting Information). Table S1 (Supporting Information) contains the thickness values of the films for different intercalants measured by AFM.

2.2. Electrical and Optical Properties of $Ti_3C_2T_x$ Films

The DC sheet conductance of films was measured with a 4-point probe and plotted against the thickness measured by AFM (**Figure 3a–d**). In all cases, a linear fit was observed, suggesting that the films exhibit bulk-like transport even for small thicknesses. One batch of $Ti_3C_2T_x$ was delaminated with LiCl (further labeled as LiCl*) and used as a precursor for protonated and sonicated samples. This batch showed higher conductance and the same surface roughness, resulting in a DC conductivity value of 18.4×10^5 S m^{-1} ($R^2 = 0.827$). One set of five films was used as a control, while another was used for preparing the protonated samples. Despite the change in interlayer spacing by 0.7 Å, the conductivity values did not noticeably change within the error of measurement after protonation, with a conductivity of 17.0×10^5 S m^{-1} (Figure 3a). Due to the synthesis process being dependent on various parameters, some batch-to-batch deviations are expected, as observed for the second batch of LiCl-intercalated film demonstrating a conductivity value of 8.50×10^5 S m^{-1} ($R^2 = 0.952$) (Figure 3b), in agreement with similar systems previously reported.[14,41] This solution was used as a precursor for intercalating larger molecules, such as TMAOH and TBAOH. Films produced from TMAOH and TBAOH solutions showed conductivity of 1.4×10^4 S m^{-1} ($R^2 = 0.958$) (Figure 3c) and 1.0×10^3 S m^{-1} ($R^2 = 0.988$) (Figure 3d), respectively. This is a significant decrease by a factor of 60 for TMAOH and 818 for TBAOH compared to the LiCl-intercalated films. The surface roughness of the films becomes harder to control during the deposition process due to the increased size of intercalants.

The variation of the DC conductivity of the $Ti_3C_2T_x$ film from 17.0×10^5 S m^{-1} to 1.0×10^3 S m^{-1} overlaps in its range to one reported for various other MXene compositions by Han et al.,[14] where $Ti_3C_2T_x$ exhibited the highest DC conductivity of 8.8×10^5 S m^{-1} and Nb_2C exhibited the lowest of ≈100 S m^{-1}.[14] All films have shown linear dependence of conductance on thickness, suggesting bulk-like current transport even down to 10 nm-thick films.

Optical measurements allow us to obtain information about the flake composition and losses occurring in the films. To investigate the intra-flake (short-range) electron transport, the optical properties of the films were analyzed by UV–vis spectroscopy from 300 to 1000 nm for all intercalants by measuring the sample transmission. MXene films exhibit low reflectivity in the optical range, leading to negligible scattering, which allows us to attribute the measured absorbance to absorption by $Ti_3C_2T_x$. Spectra for intercalated films are presented in Figure S2a–d (Supporting Information), demonstrating the increase in optical absorbance with film thickness. Typical spectra are plotted in **Figure 4a**. The optical absorbance peak ≈800 nm experiences slight shifts depending on intercalants, indicating that flakes maintain their surface terminations and have not been oxidized.[35,51] The absorbance at 550 nm for each sample was

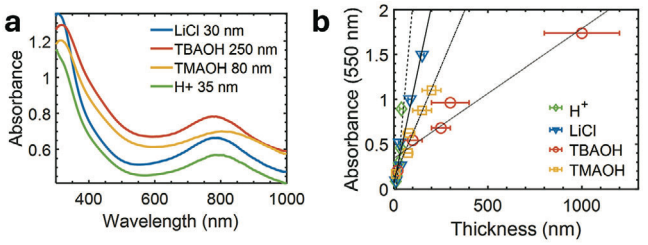

Figure 4. a) UV–vis spectra of selected samples showing similar absorbance trends. b) Absorbance at 550 nm for $Ti_3C_2T_x$ films intercalated with different agents as a function of thickness.

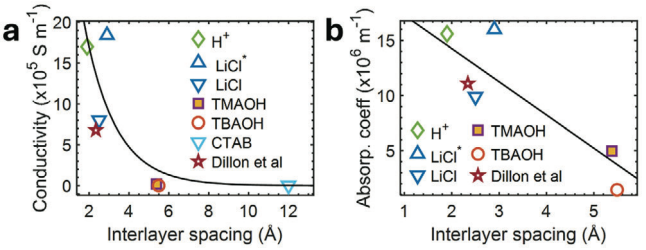

Figure 5. Dependence of electrical and optical properties on interlayer spacing. a) DC Conductivity (slopes of fitting curves from Figure 3) versus interlayer spacing for all samples under investigation. b) Optical absorption coefficient (slopes of fitting curves from Figure 4b) at 550 nm versus interlayer spacing for all samples under investigation. Results reported by Dillon et al.[41] are reported for comparison.

plotted in Figure 4b against its thickness to determine the optical absorption coefficient. These are linear for all samples, indicating a homogeneous response, allowing us to consider film properties as bulk-like up to optical frequencies.[35,41] The absorbance coefficient decreases slightly with interlayer spacing. Films with higher DC conductivity (LiCl and H^+) exhibit steeper slopes, i.e., 1.6×10^7 m^{-1} and 1.5×10^7 m^{-1}, respectively. The less conductive TMAOH and TBAOH samples have flatter slopes of 4×10^6 m^{-1} and 1.1×10^6 m^{-1}, respectively.

Although flake size might vary within different solutions due to the centrifugation[52] involved during the ion exchange, it does not affect the position of the characteristic plasmon peak; however, flake size linearly affects the optical absorbance coefficient and DC conductivity.[53] To estimate such an influence, $Ti_3C_2T_x$ solution was sonicated to decrease the flake size. The resulting solution was spray-coated and compared to the original sample (Figure S3a–d, Supporting Information). Estimation of the flake size with DLS (Dynamic Light Scattering) provides values ≈100 nm (Figure S3e, Supporting Information). Conductance is linearly dependent on thickness (Figure S4a, Supporting Information), resulting in a DC conductivity of 600 S m^{-1}, 30 times lower than the value obtained for larger flakes. Figure S4b (Supporting Information) demonstrates UV–vis absorbance spectra indicating no change of the 780 nm peak. The plot showing optical absorbance at 550 nm versus film thickness displays a linear trend and a 1.5-time decrease in absorbance coefficient from 1.6×10^7 m^{-1} to 0.8×10^7 m^{-1}, with little influence on the typical plasmon peak position (Figure S4c, Supporting Information). Variation of optoelectronic properties with flake size is summarized in Figure S4d (Supporting Information).

The change in DC conductivity and optical absorbance coefficient as a function of the interlayer spacing is plotted in **Figure 5**. In Figure 5a, conductivity decreases by three orders of magnitude when increasing the interlayer spacing, changing from 17.0×10^5 S m^{-1} to 1.0×10^3 S m^{-1} for 1.9 and 5.5 Å, respectively. CTAB-intercalated sample demonstrated DC conductivity of 1.8×10^3 S m^{-1} with interlayer spacing equal to 12.6 Å. The results were fitted with an exponential curve ($R^2 = 0.95$) $\sigma \sim \sigma_0 e^{-d}$, where d is the interlayer spacing. Values reported previously in an optoelectronics study of $Ti_3C_2T_x$ by Dillon et al.,[41] plotted in the same figure, are a close fit. While the number of data points is limited, possible exponential decay may be consistent with tunneling probability decay for metal composites,[54,55] in which metal clusters are separated from each other. In Figure 5b, absorbance coefficients for the investigated samples are plotted against the interlayer spacing. With increasing spacing, the absorbance coefficient at 550 nm linearly decreases and is fitted by a curve $\alpha = (-3.01x + 20.3)10^6\ m^{-1}$. LiCl-intercalated and protonated samples are within the same range (1.6×10^7 m^{-1} and 1.1×10^6 m^{-1}), where the minimal difference can be attributed to the slightly different morphological properties of the film (i.e., roughness). The results for LiCl-intercalated samples are in close agreement with the absorption coefficient reported by Dillon et al.[41]

2.3. Microwave Properties

The microwave performance of the films was analyzed with a waveguide at X-band (8.2–12.4 GHz) frequencies, with reflected and transmitted power values being measured through scattering parameters. The glass substrate could, in principle, affect the observed transmission and reflection. The effect of the substrate can be considered when estimating the properties of the much thinner MXene films using separately measured glass microwave properties. Since the MXene film is placed on one side of the substrate, the S_{11} and S_{22} scattering parameters (front and back reflection parameters) are not equal in general, while S_{21} and S_{12} remain equal due to reciprocity. However, as the thickness of the glass substrate decreases, its electrical length also decreases, and the values of S_{11} and S_{22} approach each other. The effect of the substrate on the measured reflection and transmission of the MXene film/substrate is negligible when S_{11} and S_{22} become equal. This is the case for the glass substrate employed in this work (thickness of ≈150 µm) (Figure S5a,b, Supporting Information).

The simplest model of a homogenous material interaction with an electromagnetic field is based on constants relating polarization and magnetization to the space-averaged electric and magnetic fields. Electromagnetic scattering parameters (S-parameters) of a slab or film based on this classical model are described in many books on electromagnetic theory. One can test the validity of the homogeneous material model by preparing sample films of different thicknesses from the material of interest, measuring the S-parameters for these samples, and comparing the experimental results to the predictions of the model. Using films of multiple thicknesses also overcomes one of the experimental difficulties in estimating the dielectric and conducting properties of very thin films. This difficulty is related to the wave phase accumulation in the material. Information obtained using material films of different thicknesses can be used to obtain

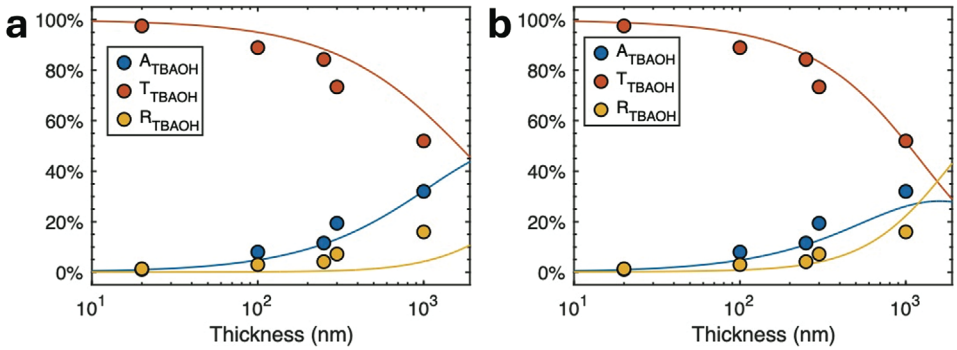

Figure 6. Analytical fitting of experimentally measured parameters based on varying conductivity and dielectric constant of MXene. Solid lines represent the theoretical curves of absorbance(blue), transmittance (red), and reflectance (yellow). a) $\sigma = 1,000\ S/m$ and $\varepsilon_r = 1$. b) $\sigma = 1,000\ S/m$ and $\varepsilon_r = 4,000$.

estimates of the dielectric constant and conductivity if the real part of the material's characteristic impedance dependent mostly on the dielectric constant is of the same order as the imaginary part dependent primarily on the conductivity. In this case, the dielectric constant and conductivity can be extracted by fitting the S-parameter model (Equations S1–S6, Supporting Information) to the measured reflected, transmitted, and absorbed power as a function of the MXene film thickness.

Figure 6 demonstrates the fitting obtained using the same conductivity and two different dielectric constants (low and high). The key feature of the model of wave propagation through a homogeneous material, that permits us to see the possible effects of the dielectric constant, is the maximum value of the absorption. When the conductivity dominates the characteristic impedance of the homogeneous material, the maximum absorption is close to 50%. This maximum can never exceed 50% which corresponds to the maximum power transfer to the material sample. As the dielectric constant increases, the absorption maximum starts to decrease. This is what appears to be happening to the absorption in Figure 6 for the lower conductivity materials, although to see a clear maximum one would have to use much thicker films.

In Figure 6, the fitting of the experimental results to the homogeneous material model appears to be better for the high relative dielectric constant of 4000, although the sensitivity of the estimate to the measured data is not high even for these relatively low-conductivity MXene films as evident from the comparison of Figure 6a,b. Additional results are presented in Figure S6 (Supporting Information), showing that the number of combinations of dielectric constant and conductivity provide a suitable fit for the experimental data. Thus, the results suggest that the high reflectivity of MXenes in many applications could be obtained with the help of a high dielectric constant, even if the conductivity is reduced. The high dielectric constant estimates here are consistent with the low-frequency results on MXene particles in percolative MXene-polymer composites (like the MXene intercalated with large organic ions) with a dielectric constant of up to 10^5 at kHz frequency range.[56]

When the wavelength is much larger than the thickness of the film, the phase accumulation within the material becomes insignificant leading to the effects of the dielectric constant being diminished leading to the model (Equations S1–S6, Supporting Information) becoming significantly simplified. In this case, the assumption that the currents induced in the material by the electromagnetic wave are distributed uniformly through the film thickness is sufficient to provide accurate fitting (Equations S7–S9).[57] The films, in this case, can be completely described by their sheet resistance, which can be expressed through the film conductivity σ and thickness t according to $R_S \approx 1/\sigma t$. When sheet resistance is equal to about half the free space wave impedance Z_0, i.e., $R_s \approx Z_0/2$, up to 50% of incoming wave power is absorbed,[32,58,59] nearly independently of frequency, polarization, and angle of incidence.

Figure 7 compares theoretical and experimental values of reflected, transmitted, and absorbed power. Theoretical curves are plotted based on the difference between free space impedance and the film impedance (the nature of the film impedance, dielectric or metallic, is not taken into account). Experimental values, on the other hand, are plotted against experimentally measured DC sheet resistance. Change in the DC sheet resistance over

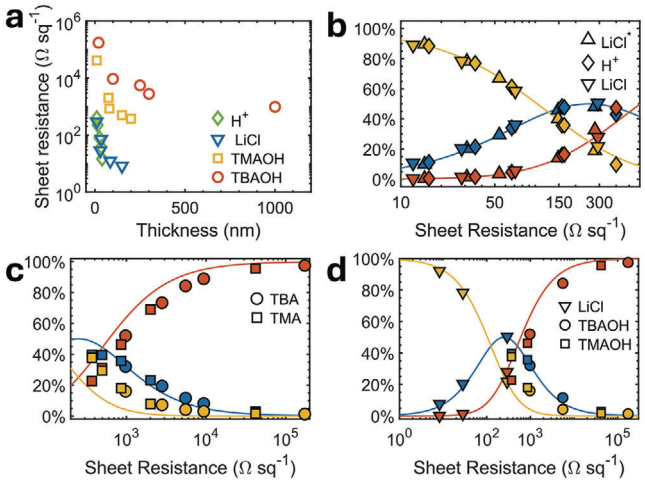

Figure 7. Microwave measurements of the absorbed, transmitted, and reflected power based on sheet resistance. Solid lines are theoretically calculated absorbance (blue), transmittance (red), and reflectance (yellow). a) Sheet resistance changes with film thickness. b) LiCl and protonated samples. c) TMAOH and TBAOH samples. d) Combined plot with selected metal- and insulator-like films highlighting the transition ≈300 Ω sq^{-1}.

thickness based on different intercalants is shown in Figure 7a. The DC sheet resistance varies drastically when changing the interlayer spacing. At thicknesses ≈15 nm, LiCl-intercalated samples have sheet resistance ≈10^2 and 10^3 times lower than TMA- and TBA-intercalated films of the same thickness, respectively. As thickness increases, the sheet resistance drops significantly for LiCl samples reaching 15 Ω sq^{-1}, while TMAOH and TBAOH show 400 and 1000 Ω sq^{-1}, respectively. Using the equations S7–S9 to correlate the scattering of the microwave signal with the impedance of the film, we can calculate theoretical curves of the microwave absorbance, transmittance, and reflectance, displayed as solid lines of blue, red, and yellow colors respectively in Figures 7b,c,d.

Due to the absence of strong frequency dependence (Figure S5c, Supporting Information), scattered microwave power was averaged over the entire frequency band. Variations along the band of measurement are due to the discontinuity of the waveguide introduced by the substrate, which can be observed in an independent measurement for the bare substrate. Deviations from frequency-averaged values are within 1–3%. Reflected, transmitted, and absorbed power for each intercalant is plotted against sheet resistance measured by a 4-point probe in Figure 5b. LiCl and H^+ samples display the same behavior close to impedance matching, occurring for films ≈10 nm thick and possessing sheet resistance of ≈180–275 Ω sq^{-1} for LiCl samples. As sheet resistance decreases to 8–15 Ω sq^{-1}, reflection becomes dominant and approaches 80%. These results agree with previously reported microwave results for $Ti_3C_2T_x$.[24] Figure 7c shows TMA- and TBA-intercalated samples with thicknesses of 15 and 20 nm being fully transmissive to microwaves with transmission ≈90% and sheet resistance of 10^5 Ω sq^{-1}, a behavior similar to a dielectric substrate. With a decrease in sheet resistance, transmittance decreases to 20% while reflectance and absorbance increase up to 40% for thicknesses of 200 nm in the case of TMAOH and 1 micron for TBAOH, corresponding to sheet resistance of 400 and 1000 Ω sq^{-1}, respectively. Films made from sonicated films demonstrated a sheet resistance change from 400 to 1000 Ω sq^{-1} for thickness values of 45 and 15 nm (Figure S7, Supporting Information), pointing to the same interaction with microwave as TMA- and TBA-intercalated films. Departure between theoretical curves and experimental data can be attributed to the frequency-dependent nature of the waveguide impedance as well as the effects of the gap introduced by the substrate and the interface between the MXene film and the waveguide flange.

Using theoretical estimations of reflected, transmitted, and absorbed power, the shielding effectiveness can be calculated and plotted against sheet resistance (Figure S8, Supporting Information). This allows us to predict the film microwave performance without microwave measurements. For composites with lower conductivity, where DC conductivity measurements by a 4-point probe may be problematic, the proposed methodology gives more accurate material parameter extraction. Absorbance, reflectance, and transmittance over a broad range of impedances are plotted in Figure 7d. Samples that are close to the impedance matching are situated around the maximum of the absorption peak. The LiCl sample with a thickness of 10 nm is close to impedance matching, while the TMAOH approaches the same absorption value at 200 nm. A shift to the left leads to conductor-like behavior, while a shift to the right indicates a dielectric-like behavior.[31,32,60,61] Despite being continuous and displaying bulk electrical and optical properties, a metal-to-insulator-like transition is observed in MXene films at microwave frequencies. Based on hindered electron transport in semicontinuous metal films, it may be reasonable to assume that the interlayer spacing is becoming comparable to the mean free path of electrons in MXene flakes. This assumption seems consistent with the estimated electron mean free path. Indeed, using theoretically calculated Fermi velocity[62] ($v_f = 5.5 \times 10^5$ m s^{-1}) and the estimated relaxation time ranging from 1 to 10 fs[23,25,62] the mean free path in $Ti_3C_2T_x$ MXene can vary from 5.5 to 55 Å. Optical estimation of the mean free path by Dilon et al.[41] was 2 nm, resulting in a relaxation time of 3–4 fs. The estimated mean free path is larger than interlayer spacing, allowing for effective electron transport from flake to flake. With such fast relaxation times, $\omega\tau \ll 1$, conductivity $\sigma = \sigma_0/(1 - i\omega\tau)$ will remain unchanged in the broad frequency range up to THz, which is supported by a combination of DC, microwave, and THz measurements. As a result, a set of continuous $Ti_3C_2T_x$ films with identical intra-flake properties and different interlayer spacings hinders electron transport, leading to the metal-to-insulator-like transition previously investigated for metal films and metallic composites.

3. Conclusion

We demonstrated that even very thin MXene films can be considered as homogeneous systems. With the increase in interlayer spacing, the material conductivity decreases. LiCl-intercalated films demonstrate metallic-like behavior and 50% microwave absorption for a thickness equal to 10 nm. Meanwhile, larger spacing due to TMAOH and TBAOH reaches 40% and 35% of microwave absorption at 200 nm-thick films and 1 µm-thick films, respectively. Therefore, controlling electron transport allows for a shift of the impedance-matching conditions to thicker films. In the microwave frequency range, this results in films changing their properties from reflective to transmissive, with a highly absorptive (up to 50%) impedance-matching condition. Decreasing MXene conductivity appears to reveal a potential effect of large dielectric constant at microwave frequencies. Optical properties are also affected by interlayer spacing as absorption coefficient values decreased linearly by an order of magnitude from 1.6×10^7 m^{-1} to 1.1×10^6 m^{-1} with an increase in the interlayer spacing. As the tunable performance of thin films is highly desirable for electromagnetic absorbers and multispectral camouflage, along with electrical conductivity, low emissivity, and stability, $Ti_3C_2T_x$, paired with ease of processibility, represents a promising candidate for such applications.

4. Experimental Section

Detailed experimental information is available in Supporting Information.

Supporting Information

Supporting Information is available from the Wiley Online Library or from the author.

Acknowledgements

This work was supported by the U.S. National Science Foundation (grants ECCS-2034114). The authors thank Prof. Aaron Fafarman and Prof. Christopher Shuck for valuable discussions, Prof. Kapil Dandekar for providing access to PNA-X, Dr. Iryna Roslyk for providing multilayer MXene, Dr. Ruocun (John) Wang for collecting the SEM images and Teng Zhang for help with protonation of the samples.

Conflict of Interest

The authors declare no conflict of interest.

Data Availability Statement

The data that support the findings of this study are available from the corresponding author upon reasonable request

Keywords

Absorber, EMI, Interlayer spacing MXene

Received: June 17, 2024
Revised: August 21, 2024
Published online:

[1] M. Naguib, M. Kurtoglu, V. Presser, J. Lu, J. Niu, M. Heon, L. Hultman, Y. Gogotsi, M. W. Barsoum, *Adv. Mater.* **2011**, *23*, 4248.
[2] G. Deysher, C. E. Shuck, K. Hantanasirisakul, N. C. Frey, A. C. Foucher, K. Maleski, A. Sarycheva, V. B. Shenoy, E. A. Stach, B. Anasori, Y. Gogotsi, *ACS Nano* **2020**, *14*, 204.
[3] M. Downes, C. E. Shuck, R. W. Lord, M. Anayee, M. Shekhirev, R. J. Wang, T. Hryhorchuk, M. Dahlqvist, J. Rosen, Y. Gogotsi, *ACS Nano* **2023**, *17*, 17158.
[4] I. Roslyk, I. Baginskiy, V. Zahorodna, O. Gogotsi, S. Ippolito, Y. Gogotsi, *Int. J. Appl. Ceram. Technol.* **2024**, *21*, 2605.
[5] A. S. Zeraati, S. A. Mirkhani, P. Sun, M. Naguib, P. V. Braun, U. Sundararaj, *Nanoscale* **2021**, *13*, 3572.
[6] T. S. Mathis, K. Maleski, A. Goad, A. Sarycheva, M. Anayee, A. C. Foucher, K. Hantanasirisakul, C. E. Shuck, E. A. Stach, Y. Gogotsi, *ACS Nano* **2021**, *15*, 6420.
[7] M. Han, D. Zhang, A. Singh, T. Hryhorchuk, C. E Shuck, T. Zhang, L. Bi, B. McBride, V. B. Shenoy, Y. Gogotsi, *Mater. Today* **2023**, *64*, 31.
[8] A. VahidMohammadi, J. Rosen, Y. Gogotsi, *Science* **2021**, *372*, eabf1581.
[9] A. Lee, M. Shekhirev, M. Anayee, Y. Gogotsi, *Graphene and 2D mater* **2024**, *9*, 77.
[10] A. Sarycheva, A. Polemi, Y. Liu, K. Dandekar, B. Anasori, Y. Gogotsi, *Sci. Adv.* **2018**, *4*, eaau0920.
[11] M. Han, Y. Liu, R. Rakhmanov, C. Israel, M. A. S. Tajin, G. Friedman, V. Volman, A. Hoorfar, K. R. Dandekar, Y. Gogotsi, *Adv. Mater.* **2021**, *33*, 2003225.
[12] O. Niksan, K. Colegrave, M. H. Zarifi, *IEEE Trans.Microw. Theory Tech.* **2023**, *71*, 698.
[13] F. Shahzad, M. Alhabeb, C. B. Hatter, B. Anasori, S. M. Hong, C. M. Koo, Y. Gogotsi, *Science* **2016**, *353*, 1137.
[14] M. Han, C. E. Shuck, R. Rakhmanov, D. Parchment, B. Anasori, C. M. Koo, G. Friedman, Y. Gogotsi, *ACS Nano* **2020**, *14*, 5008.
[15] A. Iqbal, P. Sambyal, C. M. Koo, *Adv. Funct. Mater.* **2020**, *30*, 2000883.
[16] T. Yun, H. Kim, A. Iqbal, Y. S. Cho, G. S. Lee, M.-K. Kim, S. J. Kim, D. Kim, Y. Gogotsi, S. O. Kim, C. M. Koo, *Adv. Mater.* **2020**, *32*, 1906769.
[17] O. Niksan, L. Bi, K. K. Kazemi, R. Rakhmanov, Y. Gogotsi, M. H. Zarifi, *Mater. Today* **2024**, *73*, 47.
[18] M. Han, D. Zhang, C. E. Shuck, B. McBride, T. Zhang, R. J. Wang, K. Shevchuk, Y. Gogotsi, *Nat. Nanotechnol.* **2023**, *18*, 373.
[19] A. Iqbal, T. Hassan, S. M. Naqvi, Y. Gogotsi, C. M. Koo, *Nat Rev Electr Eng* **2024**, *1*, 180.
[20] S. Habibpour, K. Zarshenas, M. Zhang, M. Hamidinejad, L. Ma, C. B. Park, A. Yu, *ACS Appl. Mater. Interfaces* **2022**, *14*, 21521.
[21] W.-T. Cao, F.-F. Chen, Y.-J. Zhu, Y.-G. Zhang, Y.-Y. Jiang, M.-G. Ma, F. Chen, *ACS Nano* **2018**, *12*, 4583.
[22] S. Wan, X. Li, Y. Chen, N. Liu, Y. Du, S. Dou, L. Jiang, Q. Cheng, *Science* **2021**, *374*, 96.
[23] G. Li, K. Kushnir, Y. Dong, S. Chertopalov, A. M. Rao, V. N. Mochalin, R. Podila, L. V. Titova, *2D Mater.* **2018**, *5*, 035043.
[24] R. Rakhmanov, C. E. Shuck, J. Al Hourani, S. Ippolito, Y. Gogotsi, G. Friedman, *Appl. Phys. Lett.* **2023**, *123*, 204105.
[25] T. Zhao, P. Xie, H. Wan, T. Ding, M. Liu, J. Xie, E. Li, X. Chen, T. Wang, Q. Zhang, Y. Wei, Y. Gong, Q. Wen, M. Hu, C.-W. Qiu, X. Xiao, *Nat. Photon.* **2023**, *17*, 622.
[26] S. M. Rossnagel, *J. Vac. Sci. Technol. A* **2003**, *21*, S74.
[27] F. O. Sequeda, *JOM* **1986**, *38*, 55.
[28] I. M. Kaganova, M. I. Kaganov, *Phys. Rev. B* **2001**, *63*, 054202.
[29] L. Moraga, C. Arenas, R. Henriquez, S. Bravo, B. Solis, *Phys. B* **2016**, *499*, 17.
[30] M. Jal/ochowski, E. Bauer, *Phys. Rev. B* **1988**, *38*, 5272.
[31] O. Pfennigstorf, A. Petkova, H. L. Guenter, M. Henzler, *Phys. Rev. B* **2002**, *65*, 045412.
[32] A. K. Sarychev, D. J. Bergman, Y. Yagil, *Phys. Rev. B* **1995**, *51*, 5366.
[33] A. Lipatov, S. Bagheri, A. Sinitskii, *ACS Materials Lett* **2024**, *6*, 298.
[34] J. L. Hart, K. Hantanasirisakul, A. C. Lang, B. Anasori, D. Pinto, Y. Pivak, J. T. van Omme, S. J. May, Y. Gogotsi, M. L. Taheri, *Nat. Commun.* **2019**, *10*, 522.
[35] K. Hantanasirisakul, M. Alhabeb, A. Lipatov, K. Maleski, B. Anasori, P. Salles, C. Ieosakulrat, P. Pakawatpanurut, A. Sinitskii, S. J. May, Y. Gogotsi, *Chem. Mater.* **2019**, *31*, 2941.
[36] M. Ghidiu, S. Kota, J. Halim, A. W. Sherwood, N. Nedfors, J. Rosen, V. N. Mochalin, M. W. Barsoum, *Chem. Mater.* **2017**, *29*, 1099.
[37] Z. Jing, J. Liu, N. Li, H. Wang, K. Wu, Y. Cheng, B. Xiao, *J. Phys. D: Appl. Phys.* **2020**, *54*, 015301.
[38] X. Zhang, X. Zhao, D. Wu, Y. Jing, Z. Zhou, *Nanoscale* **2015**, *7*, 16020.
[39] M. Xu, J. Yang, L. Liu, *Phys. B* **2019**, *560*, 146.
[40] W. Zheng, B. Sun, D. Li, S. M. Gali, H. Zhang, S. Fu, L. Di Virgilio, Z. Li, S. Yang, S. Zhou, D. Beljonne, M. Yu, X. Feng, H. I. Wang, M. Bonn, *Nat. Phys.* **2022**, *18*, 544.
[41] A. D. Dillon, M. J. Ghidiu, A. L. Krick, J. Griggs, S. J. May, Y. Gogotsi, M. W. Barsoum, A. T. Fafarman, *Adv. Funct. Mater.* **2016**, *26*, 4162.
[42] K. Hantanasirisakul, Y. Gogotsi, *Adv. Mater.* **2018**, *30*, 1804779.
[43] Y. Yang, D. Zhu, W. Yan, A. Agarwal, M. Zheng, J. D. Joannopoulos, P. Lalanne, T. Christensen, K. K. Berggren, M. Soljačić, *Nature* **2019**, *576*, 248.
[44] J. C. Maxwell-Garnett, *Philos. Trans. Royal Soc. A* **1904**, *203*, 385.
[45] D. J. Bergman, *Physics Reports* **1978**, *43*, 377.
[46] D. R. Smith, J. B. Pendry, *J. Opt. Soc. Am. B* **2006**, *23*, 391.
[47] A. Iqbal, J. Hong, T. Y. Ko, C. M. Koo, *Nano Converg* **2021**, *8*, 9.
[48] A. A. Shamsabadi, H. Fang, D. Zhang, A. Thakur, C. Y. Chen, A. Zhang, H. Wang, B. Anasori, M. Soroush, Y. Gogotsi, Z. Fakhraai, *Small Methods* **2023**, *7*, 2300568.
[49] M. Downes, C. E. Shuck, B. McBride, J. Busa, Y. Gogotsi, *Nat. Protoc.* **2024**, *19*, 1807.

[50] M. Shekhirev, C. E. Shuck, A. Sarycheva, Y. Gogotsi, *Prog. Mater. Sci.* **2021**, *120*, 100757.
[51] J. K. El-Demellawi, S. Lopatin, J. Yin, O. F. Mohammed, H. N. Alshareef, *ACS Nano* **2018**, *12*, 8485.
[52] M. Shekhirev, J. Busa, C. E. Shuck, A. Torres, S. Bagheri, A. Sinitskii, Y. Gogotsi, *ACS Nano* **2022**, *16*, 13695.
[53] K. Maleski, C. E. Ren, M.-Q. Zhao, B. Anasori, Y. Gogotsi, *ACS Appl. Mater. Interfaces* **2018**, *10*, 24491.
[54] I. Balberg, *J. Phys. D: Appl. Phys.* **2009**, *42*, 064003.
[55] D. Toker, D. Azulay, N. Shimoni, I. Balberg, O. Millo, *Phys. Rev. B* **2003**, *68*, 041403.
[56] S. Tu, Q. Jiang, X. Zhang, H. N. Alshareef, *ACS Nano* **2018**, *12*, 3369.
[57] M. Dressel, G. Grüner, *Electrodynamics of solids: optical properties of electrons in matter*, Cambridge University Press, Cambridge, New York, **2002**.
[58] W. Woltersdorff, *Z. Physik* **1934**, *91*, 230.
[59] N. Luhmann, D. Høj, M. Piller, H. Kähler, M.-H. Chien, R. G. West, U. L. Andersen, S. Schmid, *Nat. Commun.* **2020**, *11*, 2161.
[60] R. C. Hansen, W. T. Pawlewicz, *IEEE Trans. Microw. Theory Tech.* **1982**, *30*, 2064.
[61] J. Obrzut, O. Kirillov, In *2013 IEEE International Instrumentation and Measurement Technology Conference (I2MTC)*, Minneapolis, MN, USA, July, **2014**.
[62] M. Bagheri, R. Ibragimova, H.-P. Komsa, *Phys. Rev. B* **2021**, *104*, 035408.